Turbulent transport in the core of a trailing half-delta-wing vortex

By P. N. SHAH[1], P. ATSAVAPRANEE[1], T. Y. HSU[1], T. WEI[1] AND J. McHUGH[2]

[1]Department of Mechanical and Aerospace Engineering, Rutgers:
The State University of New Jersey, Piscataway, NJ 08854-8058, USA

[2]Department of Mechanical Engineering, University of New Hampshire,
Durham, NH 03824, USA

The development of a turbulent streamwise vortex core in the wake of a half delta wing has been examined using high-resolution DPIV. The objective of this work was to gain understanding of the transport processes at work a short distance downstream of the wing trailing edge as the wake vortex developed. Experiments were conducted in the Rutgers Free Surface Water Tunnel using an in-house DPIV system. A turbulent streamwise vortex was generated by a half delta wing, with 44 cm chord length and 60° sweep angle, mounted at 30° angle of attack. Reynolds number based on chord length was 65 000. Laser sheets oriented perpendicular to the flow direction were positioned 1, 3.5, and 7 chord lengths downstream of the wing trailing edge. Instantaneous vortex centres were identified in order to track vortex meandering as well as for better quantification of turbulence levels in the vortex core. Mean and fluctuating turbulence terms in the mean streamwise vorticity transport equation along with turbulent kinetic energy dissipation and production were evaluated relative to an inertial reference frame as well as relative to a vortex-centred frame. The results of this analysis highlight the importance of this near-wake region to the downstream evolution of the trailing vortices. There is a high degree of dissipation as well as streamwise vorticity convection in the very near wake which decreases rapidly with increasing distance from the trailing edge.

1. Introduction

The problem of vortices shed from lifting surfaces has been studied entensively. Much of this work has been driven by issues of flight safety associated with the persistence of tip vortices shed from large commercial aircraft. In these studies, quantification of transport processes in a turbulent streamwise vortex far downstream of the vortex generator has been of primary interest. For an extensive review of this literature, the reader is referred to Devenport *et al.* (1996). Another large body of work addresses the phenomenon of vortex bursting over the wing (generally for delta wings), including recent studies by Cipolla & Rockwell (1995) and the review of Lee & Ho (1990). There are, however, many manufacturing and aero/hydrodynamic applications in which the vortex in the near wake of a vortex generator is highly relevant. An example is the study of submarine lifting surface vortices by Shekarriz *et al* (1993). Other important technological problems requiring understanding of the near-wake structure of a trailing vortex include tail buffeting of high performance

aircraft at high angles of attack, and turbulent strain and mixing in industrial manufacturing processes such as paper making. The focus of the present work is the near-wake vortex development problem.

In spite of its importance, the evolution of trailing vortices within a few chord lengths downstream of the wing trailing edge has received, by comparison, little attention. No table exceptions are the exquisite flow visualization studies of Miller & Williamson (1995), the detailed flow measurements of Green & Acosta (1991), Devenport, et al. (1996), and Chow, Zilliac & Bradshaw and the classic theoretical analysis of Phillips (1981).

Phillips (1981) extended the theoretical work of Batchelor (1964) by considering the roll-up of a thin *turbulent* sheet of vorticity generated over a lightly loaded two-dimensional wing. In this analysis, he hypothesized the existence of three annular regions. He defined the inner region to be the solid-body core in which viscous effects dominate turbulence transport and the Reynolds stress in the cross-stream plane, defined as $-\langle u_r u_\theta \rangle$, is negative. The second region is characterized by a maximum in tangential velocity and, a change in sign of the Reynolds stress. In the third and outermost region, the individual spiralling turns of the rolling up vortex sheet are merging into a continuous smooth layer. Reynolds stresses in this region, Phillips (1981) demonstrated, approach zero as the inverse square of radius. While he commented on differences between rectangular platform wings and Δ-wings, he did not extend his analysis to heavily loaded wings in which the turbulent wing vorticity is no longer confined to an asymptotically thin sheet.

Much of the experimental data obtained close to the trailing edge have also been for rectangular planform wings. Green & Acosta (1991) studied trailing vortices from two different rectangular planform hydrofoils in a water tunnel. Using microbubbles as seeding particles, they used double pulsed holography to measure turbulence quantities in the trailing vortex cores. Very near the trailing edge, the axial velocity in the core was found to be strongly Reynolds number dependent but systematically higher than the free-stream velocity; this was consistent with the theoretical predictions of Batchelor (1964) and Saffman (1992). The axial velocity fluctuations were also found to be quite large. Large fluctuations were often due to a 'kinking' of the vortex in which the axis would momentarily diverge from the mean flow direction.

Perhaps the most detailed near-wake trailing vortex study to date was conducted by Devenport et al. (1996). They used miniature four-sensor hot wire probes to study the wake of a rectangular NACA-0012 half wing. Measurements were made between 5 and 30 chord lengths downstream of the wing trailing edge. Spectra of the fluctuating velocity signals enabled Devenport et al. (1996) to decouple the effects of turbulence from the effects of vortex meandering. Their findings were consistent with the analytical predictions of Phillips (1981), namely there was a laminar vortex core surrounded by an ever tightening spiral of wing vorticity.

Very recently, Chow et al. (1997) used triple-sensor hot wire probes to map the velocity field in cross-stream planes at various locations on and downstream of the wing. The extreme downstream measurement plane was 0.68 chord lengths aft of the trailing edge. A key finding from these measurements was that the Reynolds stress lags the mean strain rate. This indicates strong anisotropy in the near wake and, as pointed out by Chow et al. (1997) can have significant implications for turbulence modellers.

The flow field behind a delta wing at large angle of attack is very different from that of a lightly loaded two-dimensional wing. A detailed description of

trailing vortices rolling up over a delta wing in both steady and unsteady flow is given by Lee & Ho (1990). Unlike the rectangular planform wing where turbulence and vorticity are initially confined to a thin quasi-two-dimensional sheet close to the wing (which, of course, rolls up into a vortex at the wing tip), the wake of a delta wing includes a large three-dimensional low-momentum wake component. Lee & Ho (1990) pointed out that, by virtue of its geometry, the mean flow has a component which is aligned with the leading edge. This component of the flow carries leading-edge vorticity off the wing in a continuous manner and acts to keep the flow over a delta wing attached at very high angles of attack.

The performance of a delta wing is highly dependent upon whether or not the leading-edge vortex has burst. For this reason, considerable attention has been focused toward understanding the vortex bursting phenomenon over delta wings. In addition to the work of Lee & Ho (1990), a very recent paper by Honkan & Andreopoulos (1997) provides an overview of work in this field.

There are very few papers in which the near-wake evolution of a high angle of attack Δ-wing was studied. Mehta & Cantwell (1988) conducted detailed measurements behind a half Δ-wing with a 68° sweep angle at a Reynolds number based on circulation of ~ 6800. Unfortunately, the angle of attack was low, only 3°. While this is of great value in the context of Phillips' (1981) theoretical analysis, it is only of marginal utility to the present work.

Miller & Williamson (1995) conducted a laser-induced fluorescence flow visualization study of flow over and behind a delta wing. This work was recently followed by a quantitative study, Miller & Williamson (1997). In these studies, a 75° sweep angle delta wing was permitted to fly freely in a quiescent water tunnel. While the flow conditions were not explicitly stated, it appears that the Reynolds number and angle of attack were sufficiently low that coherent structures could be observed over many chord lengths downstream of the wing. However, the key difference between their work and the present study is that they specifically avoided the burst vortex condition, while the present authors were specifically interested in the burst vortex.

In the present investigation, the near-wake characteristics of a trailing vortex generated by a 60° swept half delta wing at 30° angle of attack was studied. The origins of this work were rooted in addressing fundamental mixing and flocculation control issues in paper manufacturing. As such, it was of interest to generate a stable vortex with high levels of turbulence and examine the evolving strain fields. However, in the context of high-performance aircraft, the classic 'tail buffeting' problem caused by strake vortices shed at high angle of attack interacting with vertical lifting surfaces is another problem in which the evolution of an unsteady turbulent trailing vortex close to the generator is of significant interest. The key advantage of the chosen flow conditions for this study is that, based on the work of Wentz & Kohlman (1971), 30° angle attack corresponds to maximum lift for a 60° swept wing even though the vortex bursts at the apex of the wing.

The scientific issues associated with a study of the near wake of a delta wing are primarily concerned with the question of how the vortex rolls up and how rapidly the vortex evolves toward its far-field state. Thus, the objectives of this investigation were: (i) to quantify turbulent transport in the wake of a high angle of attack delta wing, and (ii) to gain insight into the evolution in terms of vorticity and kinetic energy transport.
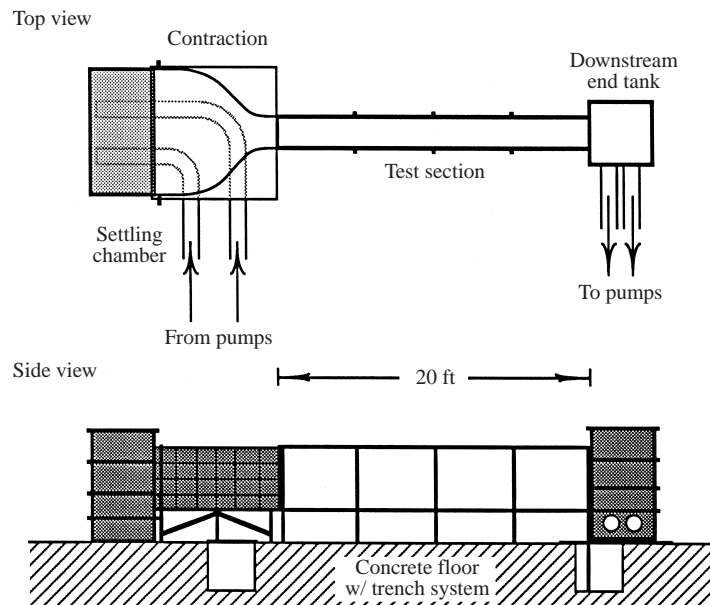
FIGURE 1. Top and side view schematic drawings of the Rutgers free-surface water tunnel. The test section is 610 cm long, 58.4 cm wide and 122 cm deep. Flow is left to right.

2. Apparatus

2.1. *Flow facility*

Experiments were conducted in the free-surface water tunnel facility at Rutgers University. Top and side view schematic diagrams of the facility appear in figure 1. The closed-circuit tunnel consisted of an upstream settling chamber, two-dimensional 4 : 1 contraction, test section, downstream end tank, pumps, and piping. Note that the pumps are not shown in figure 1. Details of the facility may be found in Grega *et al.* (1995) and Smith (1992).

The test section measured 58.4 cm in width × 122 cm in depth × 610 cm in length. It was constructed entirely from 1.91 cm thick glass panels placed in a welded steel I-beam frame. Flow was driven by two pumps operating in parallel. Variable-speed controllers were used to set the flow rate between 760 l.p.m. and 15 000 l.p.m. With the test section completely filled, the maximum flow rate corresponded to a mean free-stream velocity of approximately 30 cm s^{-1}. Free-stream turbulence levels were less than 0.1% of the mean free-stream velocity and the flow was uniform across the >7100 cm^2 cross-section to within ±2%.

2.2. *Delta wing*

The vortex generator chosen for this study was a half delta wing mounted on the sidewall of the water tunnel. The wing was constructed from a 1.27 cm thick Plexiglas plate with a 60° sweep angle and 43.9 cm chord length. Orthogonal drawings of the wing mounted in the water tunnel appear in figure 2. The chord was chosen so that the wing tip, and therefore the tip vortex, would be located roughly in the centre of the tunnel test section. The leading edge of the wing was machined with a 30° bevel on the upper surface so that there was a sharp leading edge on the underside of the wing. This is indicated in figure 2.
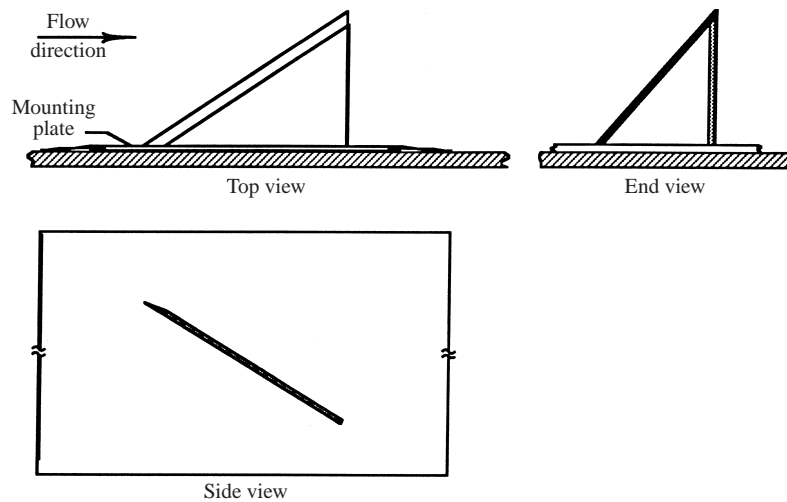
FIGURE 2. Orthographic projection of the half Δ-wing mounted along the sidewall of the water tunnel. The wing has a 60° sweep angle with a 44 cm long chord, and was mounted at 30° angle of attack to the flow direction.

The half delta wing was mounted at 30° angle of attack to the mean flow. It was bolted to a large, 45 cm long × 120 cm high × 1.27 cm thick, PVC plate mounted against one of the test section side walls ∼100 cm downstream of the inlet. To minimize step effects at the leading and trailing edges of the mounting plate, 0.16 cm thick PVC sheets were used as smoothing ramps. The projected frontal area of the wing was 275 cm^2 or 4.6% of the flow cross-section.

In order to facilitate the flow visualization studies, a dye injection slot was machined into the upper surface of the wing at the mid-span station. The slot was ∼10 cm × 0.08 cm and was oriented in the cross-stream direction. Dye was supplied through a small-diameter flexible tube which was attached from below, close to the wing root, and passed up along the test section wall behind mounting plate.

2.3. *Video imaging and capture*

Experimentation consisted of laser-induced fluorescence (LIF) flow visualization studies coupled with high-resolution digital particle image velocimetry (DPIV) measurements. In all cases fields of view were in cross-stream planes. The flow was illuminated using the beam from a Coherent Innova 70-5 5 W argon ion laser which was swept into sheets of light using a galvanometer driven by one of two laser sweep circuits. The first circuit, used for the LIF studies, generated a stepped ramp as the input signal to a galvanometer. The ensuing stepped galvanometer motion was used to generate a three-dimensional volume of equally spaced laser sheets.

The second circuit was a sweep/timing circuit used for the DPIV measurements. Its function was to generate a galvanometer input signal which would create pairs of laser sheets, one at the end of one video frame (Frame 1) and a second at the beginning of the successive frame (Frame 2); these two frames would constitute a DPIV image pair. In this manner, the effective time between frames, Δt, could be reduced to a few milliseconds even though the video system operated at 30 frames per second; in this investigation, Δt was ∼4.8 ms. One limitation of this technique, of course, is that one can only obtain image pairs at a rate of 15 Hz.

Video records of the LIF studies were made using a Sony professional video camera and SVHS recorder. For the DPIV studies, a Texas Instruments TI-1134P high-resolution black-and-white multimode video camera was used. This camera has 1134×486 pixel resolution and was configured to simultaneously image both even and odd video fields. For the final DPIV measurements, the camera was fitted with a 35 mm lens. DPIV video image pairs were captured using an EPIX 4MIP-12 video capture board. For this study the system was configured to capture an image pair, write the two image files to computer hard drive, and then capture the next image pair roughly once every five seconds. Details of the methodology appear in § 3.

2.4. *DPIV processing program*

A DPIV software package was developed for this investigation. By placing primary emphasis on accuracy (at the expense of computational speed if necessary), the resulting program could be used to compute complex turbulence quantities including terms in the turbulent vorticity and kinetic energy transport equations. Detailed documentation of the program, its calibration, and accuracy is provided in Hsu (1998); a brief uncertainty analysis is presented in the Appendix.

The essence of the program is identical to that developed by Willert & Gharib (1991). That is, cross-correlations of user-specified interrogation windows were computed in Fourier transform space to determine the mean displacement of particles contained in the windows. The principal feature of the current program is the two-step correlation process. First, a 'coarse' particle displacement field was generated using large overlapping 128 pixel $\times$ 128 pixel interrogation windows. The interrogation window in Frame 2 had the same size and location as its counterpart in Frame 1. The principal advantage of the large windows was that each window would contain many particles which would yield an accurate, albeit highly spatially averaged, displacement field.

The displacement field generated by the coarse correlation stage was then used as an initial particle displacement estimator for the 'fine' correlation stage. In this stage, interrogation windows were much smaller, as small as 16 pixels $\times$ 16 pixels. Instead of overlapping fine correlation windows, however, fine windows in Frame 2 were displaced relative to their counterparts in Frame 1 by amounts determined by local interpolation of the coarse displacement field. In this manner, it was possible to accurately compute particle displacements larger than the fine interrogation window dimensions.

For both correlation stages, zero padding and cosine windowing were used for improved accuracy. In addition, interrogation windows were moved every quarter window for an effective four times oversampling of the data. Two-dimensional Gaussian filtering (5×5 vectors) was also applied to the fine displacement field. This was done to smooth small discontinuities in the vector field with minimal additional spatial averaging over and above the four times oversampling associated with generating a vector every quarter interrogation window.

3. Experimental methods

3.1. *Flow conditions*

A series of LIF flow visualization and DPIV studies were conducted for a 60° swept half delta wing at 30° angle of attack. The free-stream velocity for this study was nominally $15\,\mathrm{cm\,s^{-1}}$ corresponding to a Reynolds number, based on free-stream velocity and chord length, of 65 000. Additional LIF flow visualization experiments

were conducted at lower Reynolds numbers as discussed in §3.2. The wing sweep angle and attitude were chosen as a function of the technological motivators for the research. Specifically, in the context of mixing, it was desirable to generate the strongest possible vortex that was stable *on* the mean. This implied maximum lift and a vortex that bursts very early in its development. Based on the work of Lee & Ho (1990), and Wentz & Kohlman (1971), the selected wing and angle of attack met those criteria. The lift coefficient for a 60° swept wing is a maximum at 30° angle of attack. Further, it has been documented that the leading-edge vortex bursts at the apex of the wing.

It is important to note that two coordinate systems are used in this paper, one centred on the wing tip, and one centred on the vortex. The vortex-centred coordinate system and manner in which data were processed in that system is described in greater detail in §3.4. Both coordinates are right-handed systems with the x-direction aligned with the mean flow, the y-direction anti-parallel to gravity, and the z-direction oriented away from the water tunnel sidewall against which the wing was mounted, i.e. in the outboard direction.

3.2. *LIF flow visualization experiments*

LIF studies were conducted over the downstream half of the delta wing for Reynolds numbers ranging from 18 000 to 65 000, the highest corresponding to that of the DPIV studies. Fluorescein dye was injected through the spanwise injection slot located at the mid-chord station of the wing. The laser sweep circuit and associated optics were configured so that a volume of eight equally spaced cross-stream sheets was swept over the downstream half of the wing, a distance of −8 cm in 0.23 s. A front surface mirror was placed in the test section well downstream of the wing at 45° to the flow direction to facilitate viewing the flow in cross-stream planes. The video camera was then, of course, oriented normal to the tunnel sidewall.

The principal objectives of the LIF work were to develop insight necessary for interpreting the DPIV data obtained downstream of the wing trailing edge, and to qualitatively determine the importance of Reynolds number on the flow. Based on the LIF results, there did not appear to be significant qualitative differences over the entire range of Reynolds numbers. It was therefore possible to use photographs taken from the 32 000 Reynolds number LIF experiment to compare with the 65 000 Reynolds number DPIV results. One advantage of this was that the effective time delay between the first and last video frames in a single three-dimensional sweep were reduced.

3.3. *DPIV measurements*

Quantitative analysis of the delta wing wake was made possible through a series of DPIV measurements in cross-stream planes located 1.0, 3.5, and 7.0 chord lengths downstream of the wing trailing edge. The fields of view for all three measurement stations were made comparatively small, approximately 5 cm × 7 cm in the vertical and horizontal directions, respectively, in order to resolve gradients of turbulent quantities in the core of the evolving vortex.

The flow was seeded by continuous circulation with 3 μm TiO_2 particles. Small amounts of additional particles were continuously injected in the settling chamber upstream of the contraction honeycomb to replace those caught in the flow conditioners or which settled along the flow loop. The affect of this injection on the delta wing flow was negligible.

Because the vortex was much larger than the field of view, preliminary large field

of view DPIV measurements were made to estimate the vortex location at each downstream measurement plane. Ensembles of over one hundred individual vector fields were averaged to identify the approximate location of the vortex centre. For the final measurements, camera fields of view were centred on the mean vortex positions found from these preliminary studies and one thousand video image pairs were captured. As noted in §2.3, successive DPIV image pairs were captured every five seconds, corresponding to approximately one vortex turnover time. The DPIV fine interrogation windows for this study were 64 pixels × 64 pixels. By generating vectors every 16 pixels, the spacing of adjacent vectors was 0.1 cm in the horizontal (z) direction and 0.16 cm in the vertical (y) direction. For comparison, the vortex core diameter is on the order of 10 cm while the Kolmogorov length scale for this flow is on the order of 0.01 cm. For the latter scale, dissipation was estimated to be the free-stream velocity cubed divided by chord length.

Two instantaneous vector fields taken one chord length downstream of the wing trailing edge are shown in figure 3. Negative distances indicate locations below and inboard of the wing tip in the y- and z-directions, respectively. The salient features of these two sample fields are their smoothness and the randomness in the instantaneous streamlines.

3.4. *Data analysis*

The first step in analysing the DPIV data was the identification and removal of bad vectors, i.e. a vector whose magnitude or direction is clearly inconsistent with its neighbours. The most common cause of bad vectors in the current program was divergence of the sub-pixel peak finding scheme. Errant vectors were generally much larger than even the free-stream velocity such that a single bad vector could affect the turbulence statistics.

Fortunately, such dramatically bad vectors were easily detected. Higher-order turbulence statistics, specifically the r.m.s. of vorticity, were very sensitive to bad vectors. By successively dividing the ensemble of vector fields in half and computing r.m.s. vorticity for each subset, it was possible to quickly find the specific instantaneous vector fields in which bad vectors resided.

Using this technique, only 68 out of the nearly four million vectors computed were found to be bad. Because of the low number, it was decided that it would be easier to simply remove the entire vector plot containing the bad vector(s) from its corresponding ensemble rather than develop a search and correction algorithm. In the worst case, this still left an ensemble of 975 vector fields with no bad vectors. The reader is again referred to the sample vector fields in figure 3.

The next step in the analysis was to compute turbulence statistics and transport terms. The most direct averaging method was to overlay individual vector fields and average quantities at identical pixel coordinates. This resulted in turbulence statistics measured relative to a stationary reference frame; for these results, the reference origin was chosen to be the wing tip. An alternative method was to find the instantaneous centre of the vortex in each DPIV realization and overlap vortex centres before averaging. This was done by ensemble averaging three consecutive vortex plots and locating the point with both minimum velocity and maximum vorticity. If such a point could not be found in a particular instantaneous vector field, then that field was not used for calculating statistics in the vortex-centred reference frame. The number of vector fields excluded by the vortex-centre finding routine was 33%, 23%, and 21% for the measurements taken at the 1.0, 3.5, and 7.0 chord lengths stations, respectively.
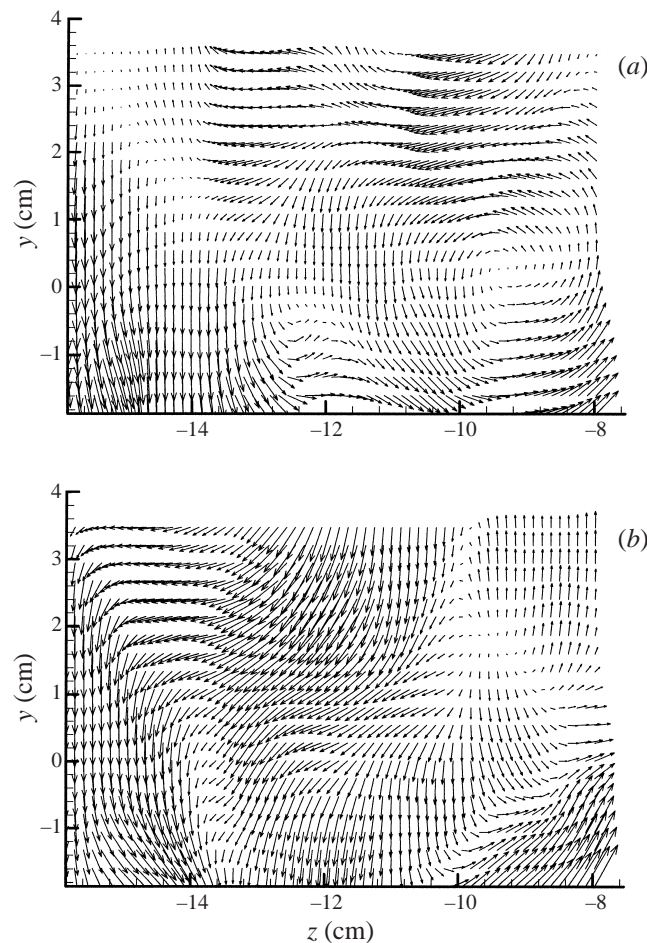
FIGURE 3. Instantaneous cross-stream velocity vector fields obtained using the DPIV program. The measurement station was located one chord length downstream of the wing trailing edge. The origin is centred on the wing tip.

4. Results

4.1. *Overview*

Flow in the near wake of a highly loaded delta wing at high Reynolds number is a complex superposition of a meandering turbulent vortex over a bluff body wake. The visualization studies of Miller & Williamson (1995) clearly show coherent structures, with vorticity aligned in the spanwise direction, in addition to the trailing vortices. These are similar to the 'striation' structures reported by Henderson & Sarpkaya (1985) and can be attributed to shear layer instabilities originating at the wing trailing edge. The existence and apparent strength of organized spanwise vorticity in the near wake highlights the importance of bluff-body features in this flow. This is an added degree of complexity not present in the lightly loaded rectangular platform wing studies of Phillips (1981), Devenport *et al.* (1996), etc. It is therefore important to remain cognizant of this coupling of effects when examining the DPIV data.

In §4.2, a combination of LIF photographs and citations from the literature serve as the basis for arguing that the vortex in this study is fully turbulent and has burst

at the apex of the wing. As previously noted, examination of the velocity field data is somewhat more problematic. One can view the turbulence statistics in an inertial frame by directly overlaying individual DPIV vector fields; these results are presented in §4.3. In this frame, bluff body characteristics of the wake are captured, but characteristics of the trailing vortex are smeared out by vortex meandering. Finding the instantaneous vortex centre and averaging, described briefly in §4.4 and in greater detail in Shah (1998), provides a more accurate description of the vortex turbulence by removing the effect of vortex meandering. This smears out the statistics associated with the bluff body wake since averages are taken relative to the meandering vortex. However, since both the bluff body and vortex characteristics are of the same order in the near wake, neither can be completely decoupled from the other.

Because of the complexity of the flow, it would therefore be useful to list key results in advance of their presentation in this section. These are the results upon which the subsequent discussion will be based. The key features of the vortex are:

 (i) the trailing half-delta-wing vortex is everywhere turbulent, having burst near the apex of the wing;

 (ii) at one chord length downstream of the wing, the mean vortex shape is a vertically oriented ellipse, with vertical mean and fluctuating velocities larger than corresponding spanwise motions;

 (iii) at seven chord lengths downstream, the vortex has evolved to a nearly circular cross-section;

 (iv) turbulence levels, including Reynolds stress, decrease dramatically between the 1 and 7 chord stations.

4.2. *Flow visualization over the wing*

Meaningful interpretation of the near-wake measurements first required knowledge about the state of the vortex over the wing. That is: was it turbulent, had it burst, was it stable, etc. To answer these questions, a series of LIF flow visualization studies was conducted. As stated in §3.2, a range of flow speeds was examined without qualitative evidence of Reynolds number effects. For image quality reasons, therefore, images from a lower, $Re = 32\,000$, Reynolds number case are presented here.

Figure 4 contains two photographs from a single 'three-dimensional image' of the flow over the downstream half of the half delta wing. The photographs were obtained from a video record in which a cross-stream laser sheet was swept along the stream direction starting at the wing trailing edge and ending at the mid-chord station. The time between the two images is 200 ms corresponding to a streamwise spacing of ~ 6 cm. The mean flow direction is out of the page, and the wing root is aligned with the left side of the photographs. Figure 4(*a*) corresponds to the mid-chord location and figure 4(*b*) was taken close to the wing trailing edge.

The important conclusion from the LIF studies is that flow over the entire wing appears turbulent. Close examination of the video tapes indicates a large, stable but turbulent, wing vortex which has burst close to the Wing apex. As pointed out by one reviewer, the nominal Reynolds number of this study, $Re = 65\,000$, is low to moderate in the context of turbulent external flows. As such, the appropriateness of calling the flow fully turbulent may be in doubt, as well as the applicability of the current data set to much higher Reynolds number flows. Nontheless, these visual observations are consistent with findings reported by Wentz & Kohlman (1971) and Lee & Ho (1990) who reported that for a 60° swept wing at 30° angle of attack, the lift coefficient is a maximum and the turbulent trailing vortex bursts at the wing apex. With this in mind, it was then possible to proceed to the near-wake DPIV measurements.
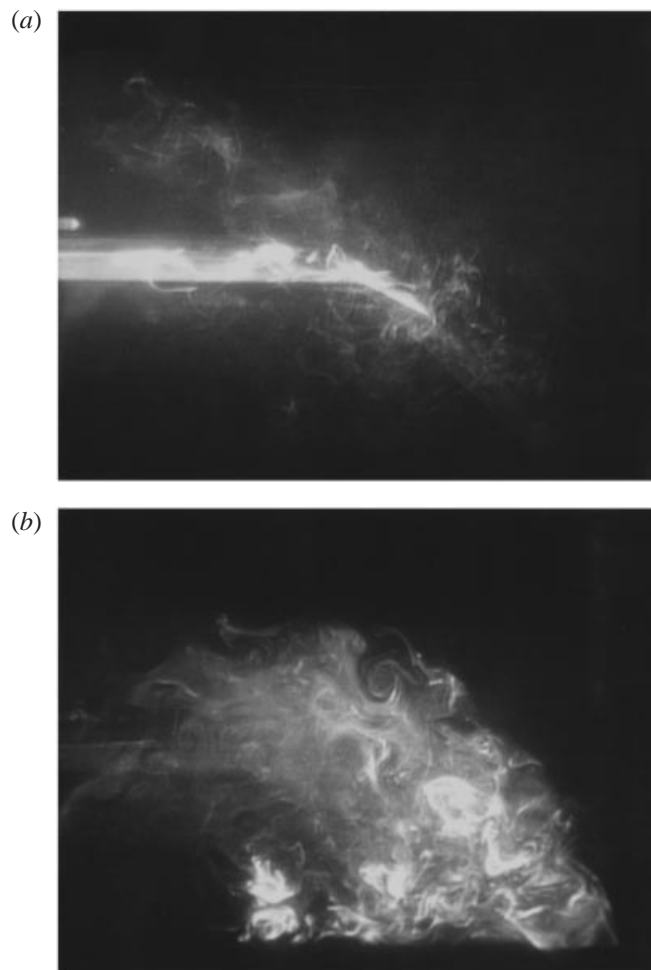
(*a*)

(*b*)

FIGURE 4. Two sample photographs from a single three-dimensional visualization of flow over the downstream half of the half Δ-wing. The root is out of view on the left of the photographs. Flow at the mid-chord and trailing-edge stations are shown in (*a*), and (*b*), respectively.

4.3. *DPIV results in an inertial reference frame*

The simplest method of analysing the DPIV data was to overlay individual fields for each downstream measurement station and compute ensemble-averaged turbulence quantities. This provided data in inertial reference frames for each of the three streamwise locations. The disadvantage of this approach is that vortex turbulence statistics are smeared by unsteady vortex motions. However, the turbulent transport equations, e.g. vorticity, kinetic energy, etc., are commonly derived for inertial frames. Consequently analysis of the data in this reference frame is essential for evaluating turbulent transport terms. This is done in § 5.

Mean cross-stream vector fields in an inertial frame for the three downstream measurement stations are shown in figure 5. Corresponding contour plots of constant spanwise and vertical mean velocities are shown in figure 6. For both figures, the origin is centred on the wing tip with negative y and z values corresponding to locations below and inboard of the wing tip, respectively. Unless otherwise noted, data for these
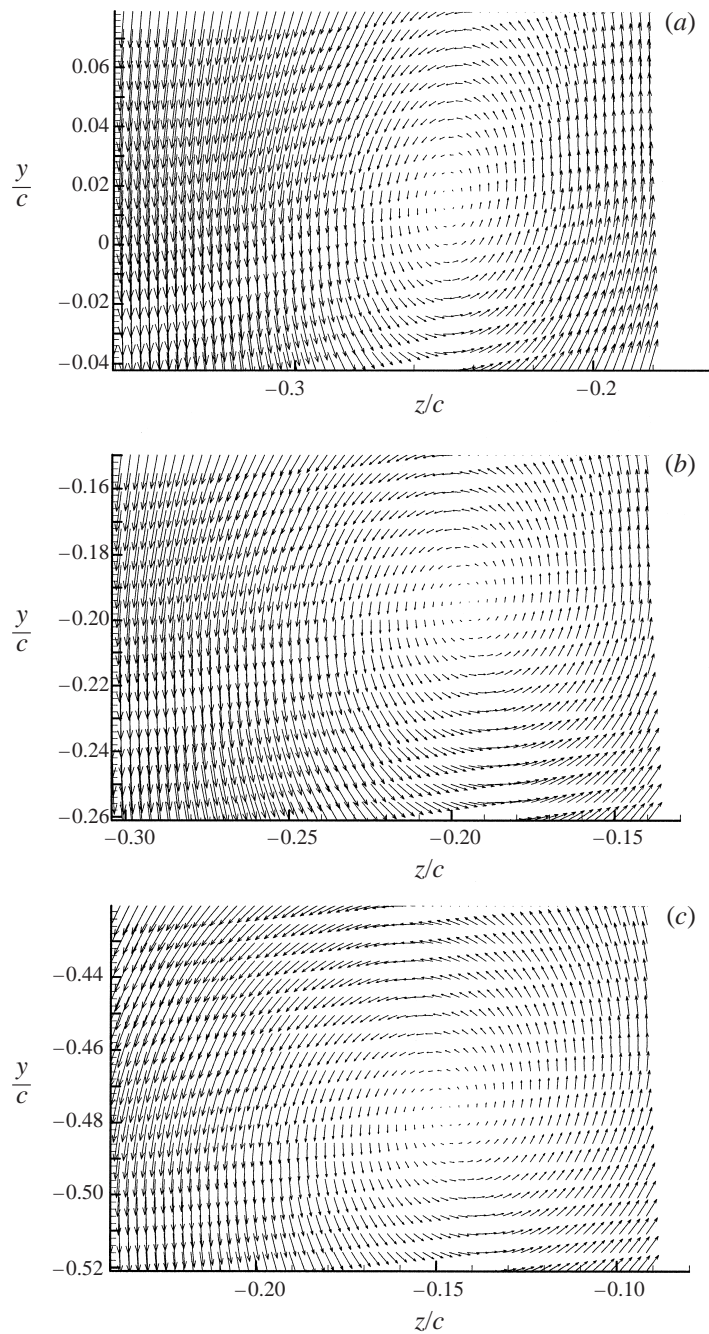
FIGURE 5. Mean cross-stream velocity vector plots for the three measurement stations $x/c = 1.0$ (*a*), 3.5 (*b*), and 7.0 (*c*). Approximately 1000 individual realizations were averaged in an inertial reference frame for each plot.

and all subsequent plots have been non-dimensionalized using free-stream velocity and chord length.

Given the nominally circular streamlines for the cross-stream plane, it was also worth while computing statistics in polar coordinates. For these calculations, the
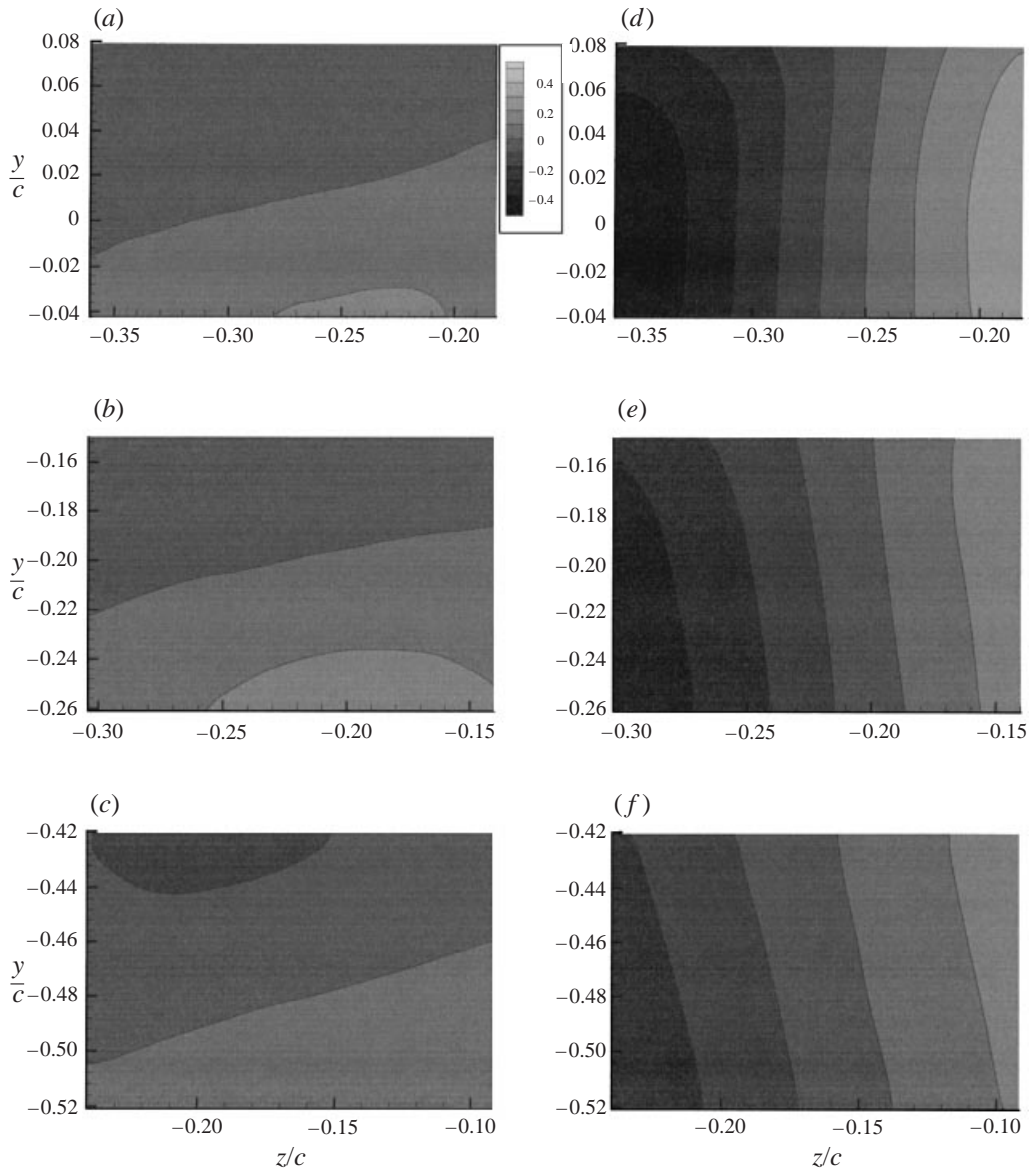
FIGURE 6. Contours of mean spanwise ($x/c = 1.0$ (*a*), 3.5 (*b*), and 7.0 (*c*)), and vertical ($x/c = 1.0$ (*d*), 3.5 (*e*), and 7.0 (*f*)) velocity relative to an inertial reference frame. This and all subsequent plots have been non-dimensionalized by free-stream speed and chord length.

centre of the mean vortex at each measurement station, shown in figure 5, was determined and used as the origin for computing position and decomposing local velocity vectors into polar components. For the complete data set, the reader is referred to Shah (1998). Only mean circumferential and radial velocity contour plots are presented in this paper.

A key feature of the mean velocity data, shown in figures 5–7, is the evolution of the Δ-wing-vortex cross-section from an ellipse, one chord length downstream of the trailing edge, to a more circular shape 7 chord lengths downstream. Eccentricity of the vortex is most evident in the mean circumferential velocity contours shown
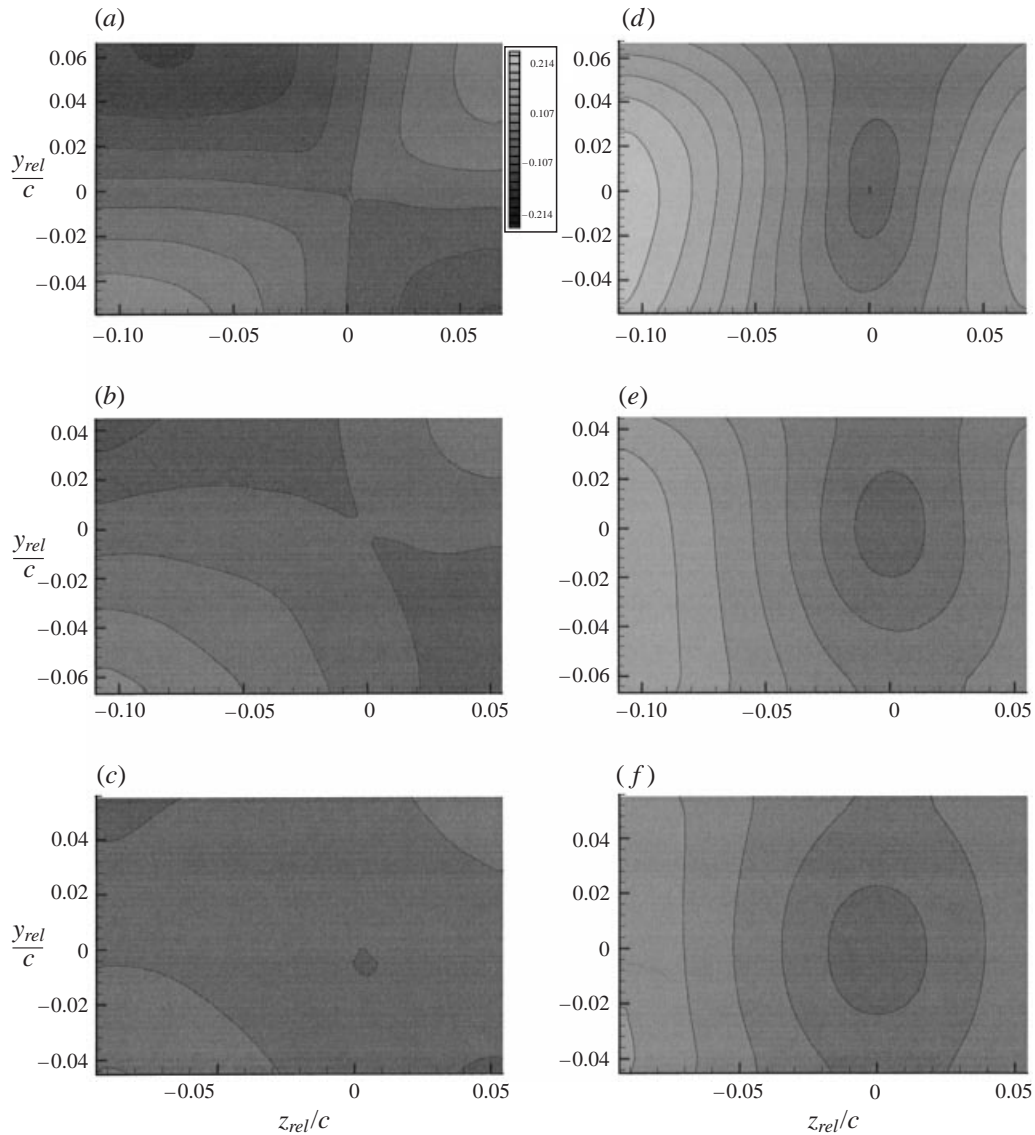
FIGURE 7. Contours of mean radial ($x/c = 1.0$ (*a*), 3.5 (*b*), and 7.0 (*c*)) and circumferential ($x/c = 1.0$ (*d*), 3.5 (*e*), and 7.0 (*f*)) velocity components for the mean vector fields shown in figure 6. The cylindrical coordinate system in centred on the mean vortex centre.

in figure 7. In Cartesian coordinates, vertical eccentricity of the vortex is manifested as strong vertical mean flows at 1 chord length as seen in figure 6. Quadranting of the mean radial velocity contours is also an artifact of the elliptical vortex shape. A vertically oriented elliptical vortex rotating in a counterclockwise direction has radially outward flow in the first and third quadrants and radial inflow in the second and fourth quadrants.

It should also be pointed out that the maximum velocity magnitudes are located at the perimeters of the mean velocity plots. This indicates that the fields of view were limited to the centre of the vortex core. Little or no information about the interaction of the core with the outer flow is available from this investigation.
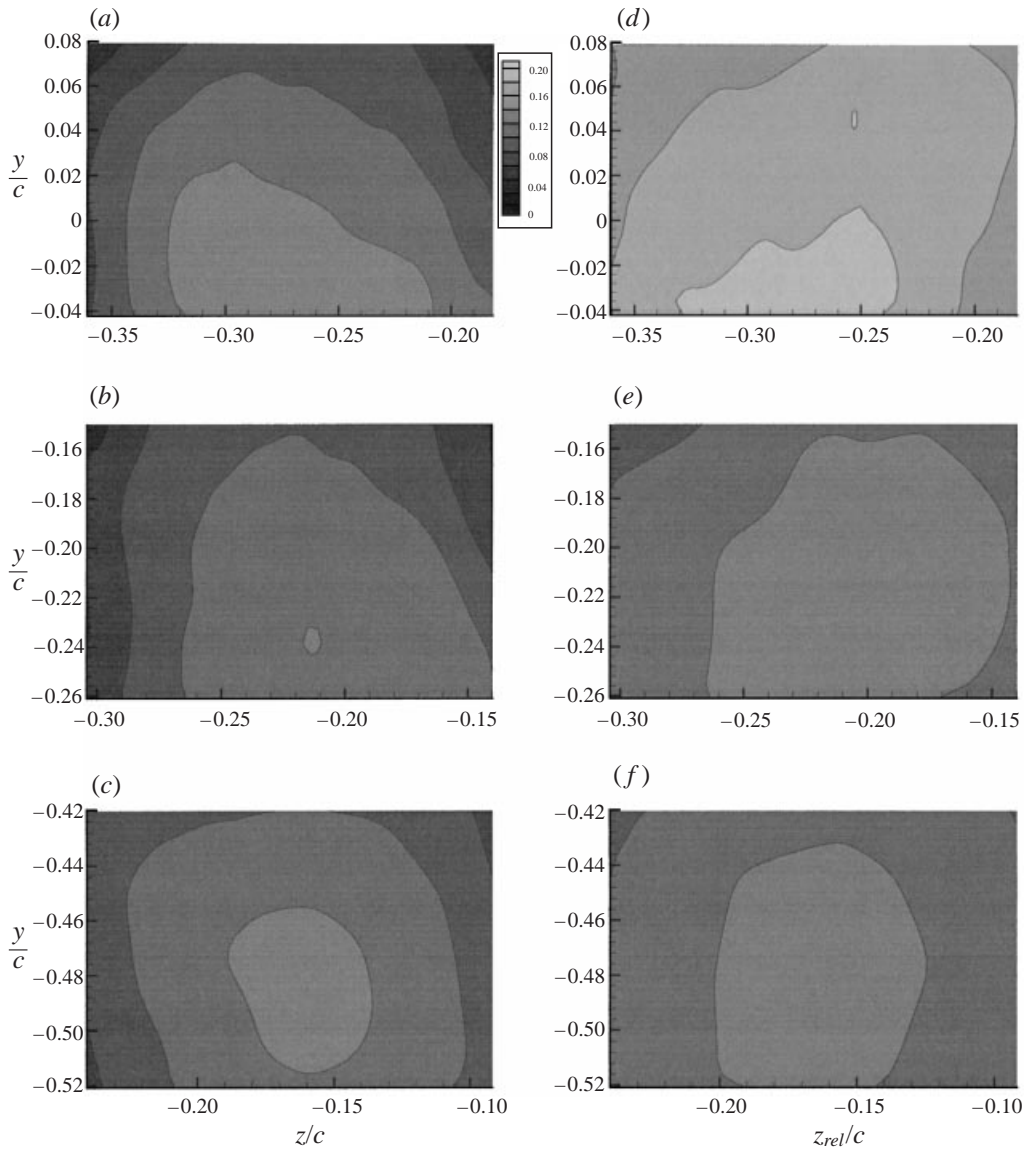
FIGURE 8. Contours of cross-stream turbulence intensities, w' ($x/c = 1.0$ (a), 3.5 (b), and 7.0 (c)) and v' ($x/c = 1.0$ (d), 3.5 (e), and 7.0 (f)), in an inertial reference frame.

Dominance of the vertical motions in the wing near wake is also visible in the turbulence intensities. Figure 8 shows the spanwise and vertical turbulence intensities, scaled on free-stream velocity and chord length, for the three measurement stations. Observe that at 1 chord length, the vertical velocity fluctuations are approximately 50% greater than the spanwise fluctuations. In contrast, further downstream at 3.5 and 7.0 chord lengths, the two components are approximately equal.

The eccentricity of the trailing vortex close to the wing trailing edge also impacts contours of constant Reynolds stress. Distributions of Reynolds stress are plotted in figure 9, non-dimensionalized by the product of the local cross-stream turbulence intensities, v' and w'. In both plots, the magnitude of maximum Reynolds stress
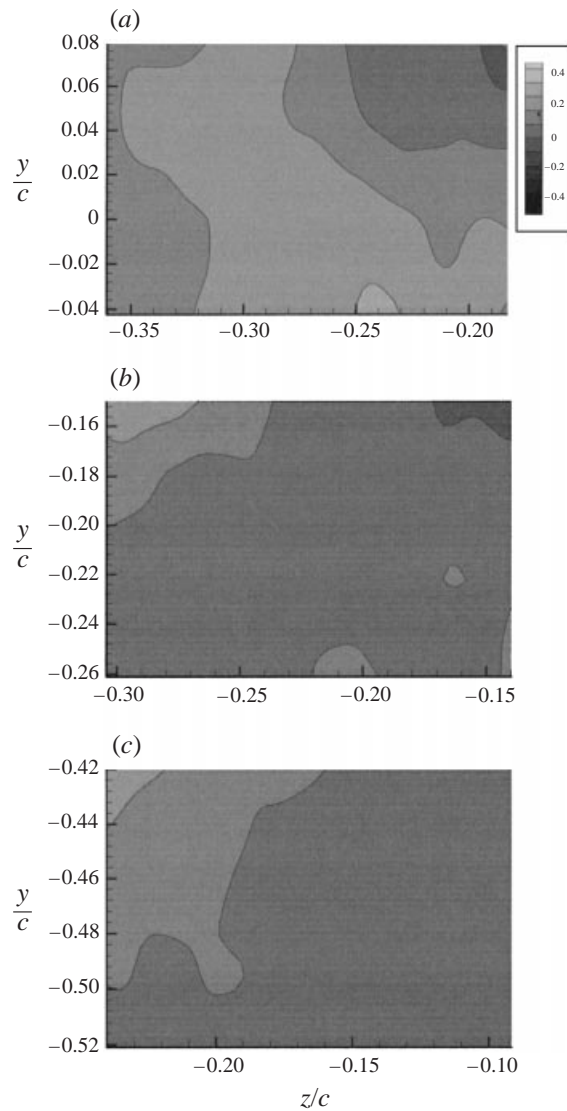
FIGURE 9. Cartesian Reynolds stress contours, $\langle vw \rangle / v'w'$ ($x/c = 1.0$ (a), 3.5 (b), and 7.0 (c)), relative to an inertial frame.

decreases dramatically from the 1 to the 7 chord length stations. In addition, it is readily apparent that the Reynolds stress distributions are everywhere positive.

Positive Reynolds stress in the Cartesian reference frame can be better understood by examining the mean velocity contours in figure 6. Observe that the vertical velocity contours are essentially vertical bands with values increasing from left to right. In contrast, contours of constant spanwise velocity are aligned horizontally and increase from top to bottom. A critical piece of information lies in mean velocity gradients, i.e. the spacing between contour lines. Owing to the vertical orientation of the vortex ellipse, the spacing between adjacent contours is smaller for the vertical velocity than the horizontal velocity. Therefore positive unit spanwise fluctuations, on average, correspond to large negative vertical fluctuations, i.e. positive Reynolds

stress. Conversely, a positive unit vertical fluctuation would result in a comparatively smaller positive spanwise fluctuation. Thus, on average, one would expect positive Reynolds stress throughout the core of the vertical-ellipse turbulent vortex. As the vortex evolved to a more circular shape with increasing distance downstream, the Reynolds stress values should reduce to zero. This is in fact the case: dimensionless Reynolds stress values in the vortex centre at the one chord station are roughly three to four times larger than at the seven chord measurement station.

4.4. *DPIV results in the vortex-centred frame*

Unsteady motions of trailing vortices are, if nothing else, an experimental complication obscuring the true nature of the vortex. A distinct advantage of the DPIV technique is that it is possible to identify the vortex centre in each instantaneous realization and thereby track the time-dependent meandering. By identifying the instantaneous vortex centre and using that centre as a common origin for all of the individual DPIV realizations, a more accurate description of the turbulence in the vortex core could be obtained. The vortex-centre-finding algorithm was described in §3.4. As an example of this capability, mean streamwise vorticity distributions for the three measurement stations appear in figure 10. It is immediately obvious that there are no qualitative differences between the inertial- and vortex-centred reference frames. However, the removal of spatial averaging effects by co-locating instantaneous vortex centres results in a tighter, higher energy core, but the shape and distribution of the vortex are unchanged. For a complete set of data in this frame, please see Shah (1998).

5. Discussion

Detailed cross-stream DPIV measurements in the near wake of a 60° swept half delta wing at 30° angle of attack were made in conjunction with scanning LIF flow visualization studies over the aft portion of the wing. The key results from this investigation were outlined in §4.1 and presented in detail in the remainder of the section. In brief, the data show that the vortex is fully turbulent beginning at the wing apex, and evolves from a vertically oriented ellipse one chord length downstream of the wing trailing edge to a near circular shape seven chord lengths behind the wing. In the process, the vorticiy contained in the core decreases significantly. The objective of this section is to discuss the evolutionary process. Specifically, turbulent transport processes will be examined in the context of the streamwise vorticity equation and the turbulent kinetic energy transport equation. The conclusions to be drawn from this analysis will be that the vortex evolution to a circular cross-section is a combination of vorticity reorientation and high levels of dissipation close to the wing trailing edge.

5.1. *Vortex evolution in the context of vorticity transport*

The mean turbulent streamwise vorticity transport equation in an inertial reference frame is

$$
\begin{aligned}
&\underset{\text{I}a}{U\partial\Omega_x/\partial x} + \underset{\text{I}b}{V\partial\Omega_x/\partial y} + \underset{\text{I}c}{W\partial\Omega_x/\partial z} = \underset{\text{II}a}{\Omega_x\partial U/\partial x} + \underset{\text{II}b}{\Omega_y\partial U/\partial y} + \underset{\text{II}c}{\Omega_z\partial U/\partial z} \\
&\quad + \underset{\text{III}a}{v\partial^2\Omega_x/\partial x^2} + \underset{\text{III}b}{v\partial^2\Omega_x/\partial y^2} + \underset{\text{III}c}{v\partial^2\Omega_x/\partial z^2} + \underset{\text{IV}a}{\partial/\partial x\{\partial\langle uv\rangle/\partial z - \partial\langle uw\rangle/\partial y\}} \\
&\quad + \underset{\text{IV}b}{\partial^2/\partial y\partial z\{\langle v^2\rangle - \langle w^2\rangle\}} + \underset{\text{IV}c}{\{\partial^2/\partial z^2 - \partial^2/\partial y^2\}\langle vw\rangle}, \quad\quad (1)
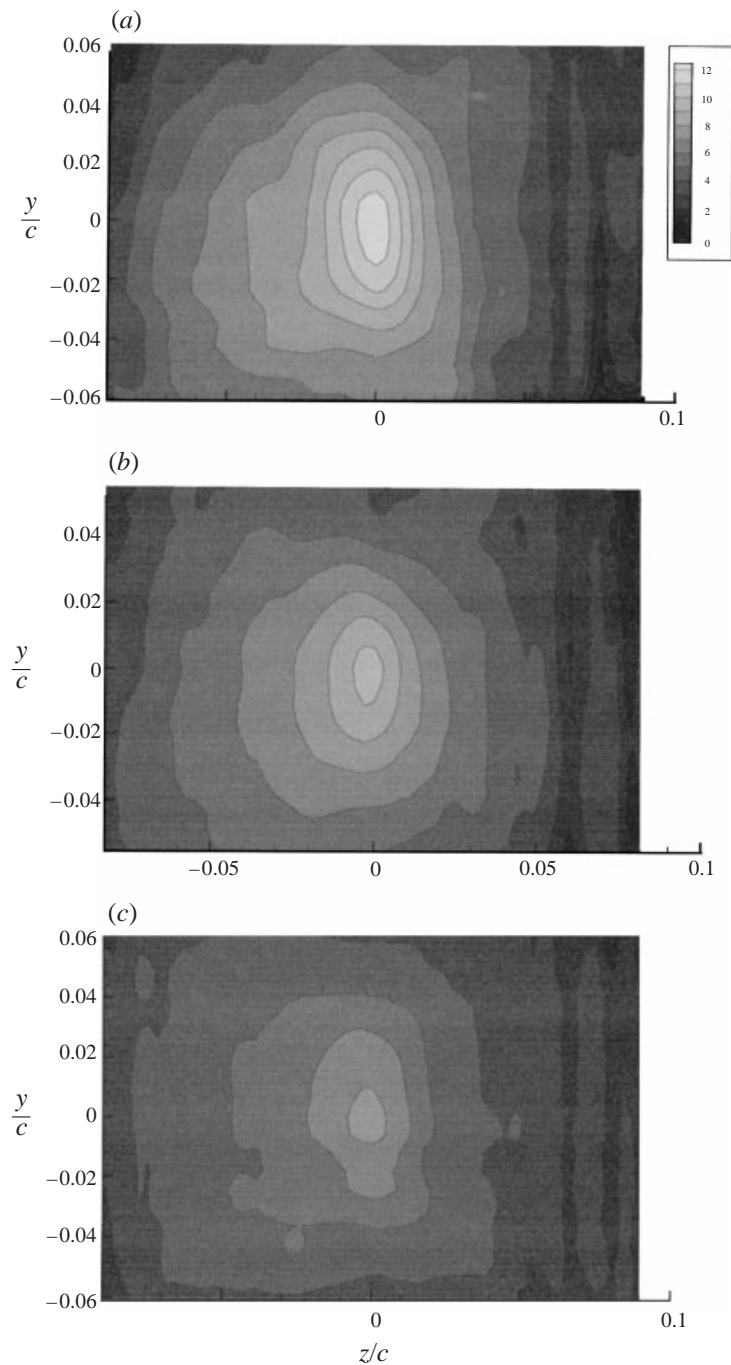\end{aligned}
$$

FIGURE 10. Mean streamwise vorticity contours, $x/c = 1.0$ (*a*), 3.5 (*b*), and 7.0 (*c*), computed using a vortex-centred reference frame.

where capital letters indicate mean quantities and angle brackets contain correlations of fluctuating velocities, i.e. Reynolds shear and normal stresses. Equation (1) results from taking the curl of the fully turbulent momentum equations and then averaging. Vorticity production terms caused by Reynolds stress production, labelled

IVa–IVc, result from simplifying the fluctuating counterparts of the vorticity stretching/reorientation terms labelled as IIa–IIc. Terms on the left-hand side of the equation describe vorticity advection following a fluid element relative to an inertial reference frame, and the terms labelled IIIa–IIIc represent diffusion of streamwise vorticity.

Obviously, it is not possible to compute all of the terms in (1) with only cross-stream velocity data. However, much insight can be obtained from those terms that can be evaluated. These include two advection terms, Ib and Ic (which are shown in figure 11), the mean stretching term, IIa†, the sum of the two diffusion terms, IIIb and IIIc, and two anisotropic Reynolds stress production terms, IVb and IVc. From the vorticity transport balance, the unresolvable terms may be lumped into a residual, $\mathscr{R}$ containing Ia, IIb, IIc, IIIa and IVa. As with other plots, figure 11 contains contour plots for each of the three downstream measurement stations using the inertial reference frame. For reasons of economy of space, data for only the two advection terms are presented here. The other measurable terms were all found to be more than an order of magnitude smaller than the vertical advection term; the residual, therefore, is qualitatively and quantitatively similar to figure 11(*a–c*). For the complete data set, the reader is again referred to Shah (1998); a brief uncertainty analysis is presented in the Appendix.

The salient feature of figure 11 is that vertical advection, $V\partial\Omega_x/\partial y$, figure 11(*a*), dominates all of the terms that could be evaluated. Observe that there is a region of strong advection in the upper left corner of the field corresponding to the inboard, or root, side of the wing where the downflow would be expected to be strongest. Since all other measurable terms are negligibly small, it follows that the term which balances $V\partial\Omega_x/\partial y$ can be found in the residual, $\mathscr{R}$.

It is hypothesized that the specific balancing term is spanwise vorticity reorientation, $\Omega_z\partial U/\partial z$. Physical arguments based on local isotropy can be made to neglect the diffusion term, III*a*, and the anisotropic Reynolds stress production term, IV*a*. The assumption that streamwise gradients are significantly smaller than cross-stream gradients makes it possible to also neglect streamwise advection, $U\partial\Omega_x/\partial x$, relative to vertical advection.

This therefore leaves the two vorticity reorientation terms, II*b* and II*c* in (1). It is argued that the reorientation and stretching of spanwise vorticity dominates that of vertical vorticity because both $\Omega_z > \Omega_y$ and $\partial U/\partial z > \partial U/\partial y$, so that necessarily $\Omega_z\partial U/\partial z > \Omega_y\partial U/\partial y$. The assumption that $\Omega_z > \Omega_y$ is supported by the present flow visualization studies as well as those of Henderson & Sarpkaya (1985) and Miller & Williamson (1995) which all show strong spanwise vortices in the wing wake and no comparable vertical sources or vorticity.

With regard to the assumption that $\partial U/\partial z > \partial U/\partial y$, examination of the mean cross-stream velocity components, shown in figure 7, clearly indicates that gradients in the spanwise direction are stronger (i.e. contour spacings are much smaller in the *z*-direction) than vertical gradients. This is probably due to the presence of the wing mounting wall, or in the case of a full symmetric delta wing, the wing symmetry plane. It is therefore assumed that the spanwise gradients of mean streamwise velocity will also be larger than the vertical gradients. An alternative way of reaching the same conclusion is to consider the fact that the vortex shape is a vertical ellipse. For such a vortex, spanwise gradients are likely to be stronger than gradients in the vertical direction. Thus, the conclusion is drawn that the vertical advection of

† Note that the mean streamwise velocity gradient can be computed from the continuity equation.
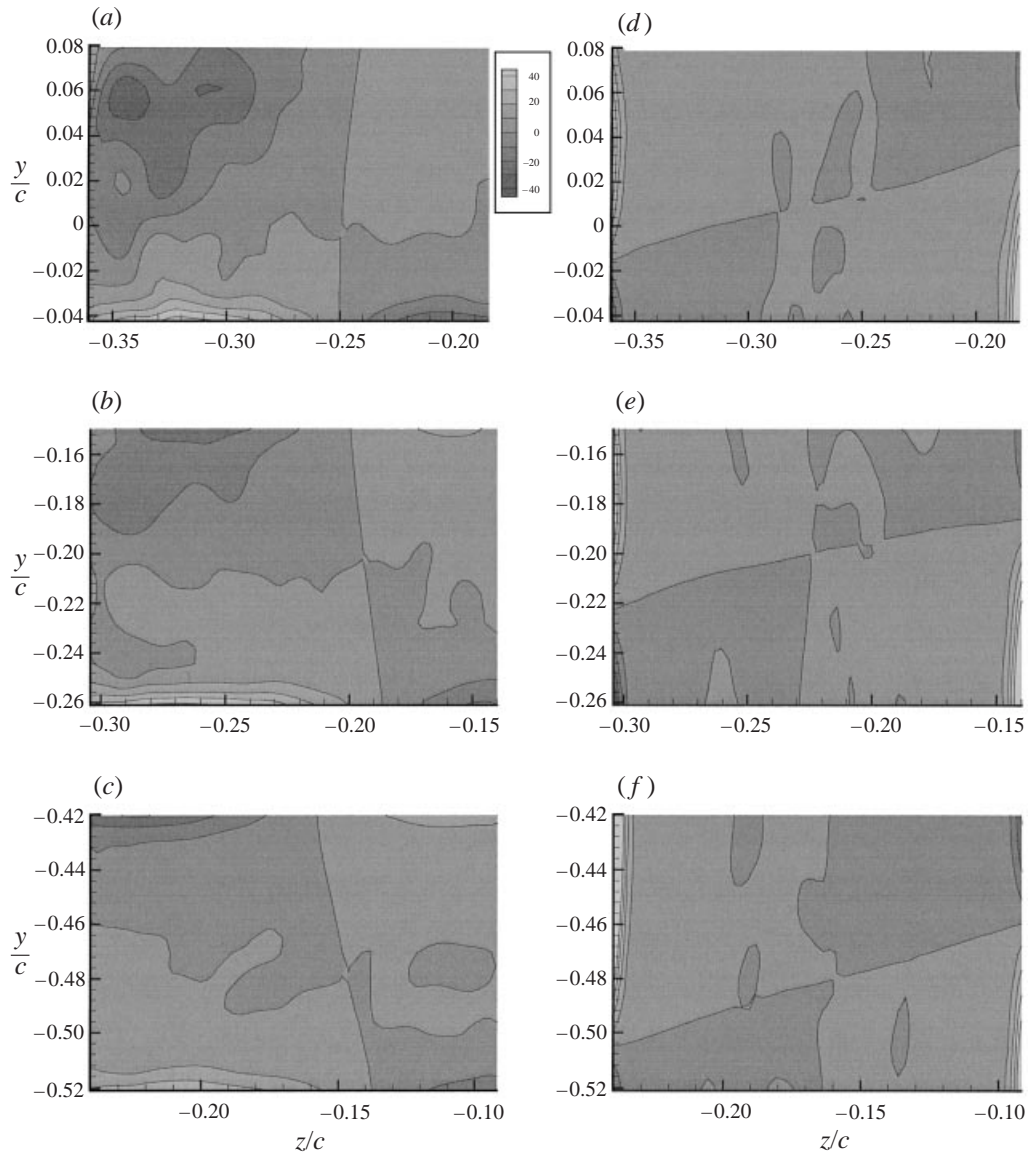
FIGURE 11. Mean vorticity advection terms, $V \partial \Omega_x / \partial y$ ($x/c = 1.0$ (*a*), 3.5 (*b*), and 7.0 (*c*)) and $W \partial \Omega_x / \partial z$ ($x/c = 1.0$ (*d*), 3.5 (*e*), and 7.0 (*f*)), computed from data in the inertial reference frame.

streamwise vorticity is balanced by the reorientation of spanwise vorticity by the spanwise gradient of mean streamwise velocity.

5.2. *Vortex evolution in the context of turbulent kinetic energy transport*

An alternative explanation of the trailing vortex evolution may be developed through examination of the turbulent kinetic energy transport equation. The advantage of this approach is that the dissipative nature of the vortex turbulence is directly considered; recall that Phillips' (1981) analysis of a turbulent vortex shed from a lightly loaded rectangular wing led the conclusion that dissipation was the dominant mechanism in

the vortex core. In this context, the balance between production and dissipation is of particular interest to this investigation.

As with vorticity transport, it was not possible to compute all of the components in the turbulence production, $\langle u_i u_j \rangle \partial U_i / \partial x_j$, and dissipation, $v \langle \{ \partial u_i / \partial x_j + \partial u_j / \partial x_i \}^2 \rangle$, terms from cross-stream data only. Specifically, only the production components, $\langle v^2 \rangle \partial V / \partial y$, $\langle w^2 \rangle \partial W / \partial z$, $\langle vw \rangle \partial V / \partial z$, and $\langle vw \rangle \partial W / \partial y$, and the dissipation components, $2v \langle \{ \partial v / \partial y \}^2 \rangle$, $2v \langle \{ \partial w / \partial z \}^2 \rangle$, and $v \langle \{ \partial v / \partial z + \partial w / \partial y \}^2 \rangle$, could be computed from the cross-stream plane DPIV velocity fields. However, comparison of these quantities provides a qualitative balance between the production and dissipation of turbulence as a function of distance downstream of the wing trailing edge. The sums of the measurable dissipation and production terms for each of the three downstream stations are shown in figure 12, non-dimensionalized by the free-stream speed cubed divided by chord length.

Comparison of the dissipation plots, figure 12(*a–c*), with the corresponding production plots, figure 12(*d–f*), immediately highlights the fact that dissipation one chord length downstream of the wing is significantly larger than at the subsequent downstream stations. It is also larger than the production, which is uniformly small for all three measurement stations. Thus, with the caveat that these are incomplete quantities, it appears that dissipation dominates the energy balance at one chord length where the vortex is elliptical in cross-section. Taken *in toto*, then, the evolution of the trailing vortex from an elliptical to circular cross-section occurs through the combined effects of spanwise vorticity reorientation and turbulent kinetic energy dissipation.

6. Conclusions

Near-wake development of a trailing vortex shed from a 60° sweep back half Δ-wing at 30° angle of attack was examined using DPIV. The objective of the investigation was to quantify turbulent transport processes in the context of both trailing vortex development and mixing in heavily loaded, fully turbulent delta wing wakes. Detailed measurements of the cross-stream turbulence between one and seven chord lengths downstream of the wing trailing edge were made in conjunction with three-dimensional LIF flow visualization studies over the aft portion of the wing. Analysis of the results led to the following conclusions:

(i) the trailing-vortex cross-section evolves from an ellipse to a circle within approximately 10 chord lengths of the wing trailing edge:

(ii) this evolution is believed to be due, in part, to the reorientation of spanwise vorticity shed from the wing trailing edge;

(iii) comparatively high levels of dissipation within one chord length of the wing also play an important role in the vortex evolution.

Appendix. DPIV measurement uncertainties

The principal goal in developing a DPIV processing program was to be able to generate accurate, high-resolution vector fields for computing complex turbulence transport quantities. To this end, the DPIV system was calibrated using a series of steps including translation and rotation of a pattern of dots as well as solid-body rotation of seeding particles in water. These tests are described in Hsu (1998). Benchmarking of this capability on a canonical flat-plate turbulent boundary layer also appears in Hsu (1998) and will be published in a separate article. In that study,
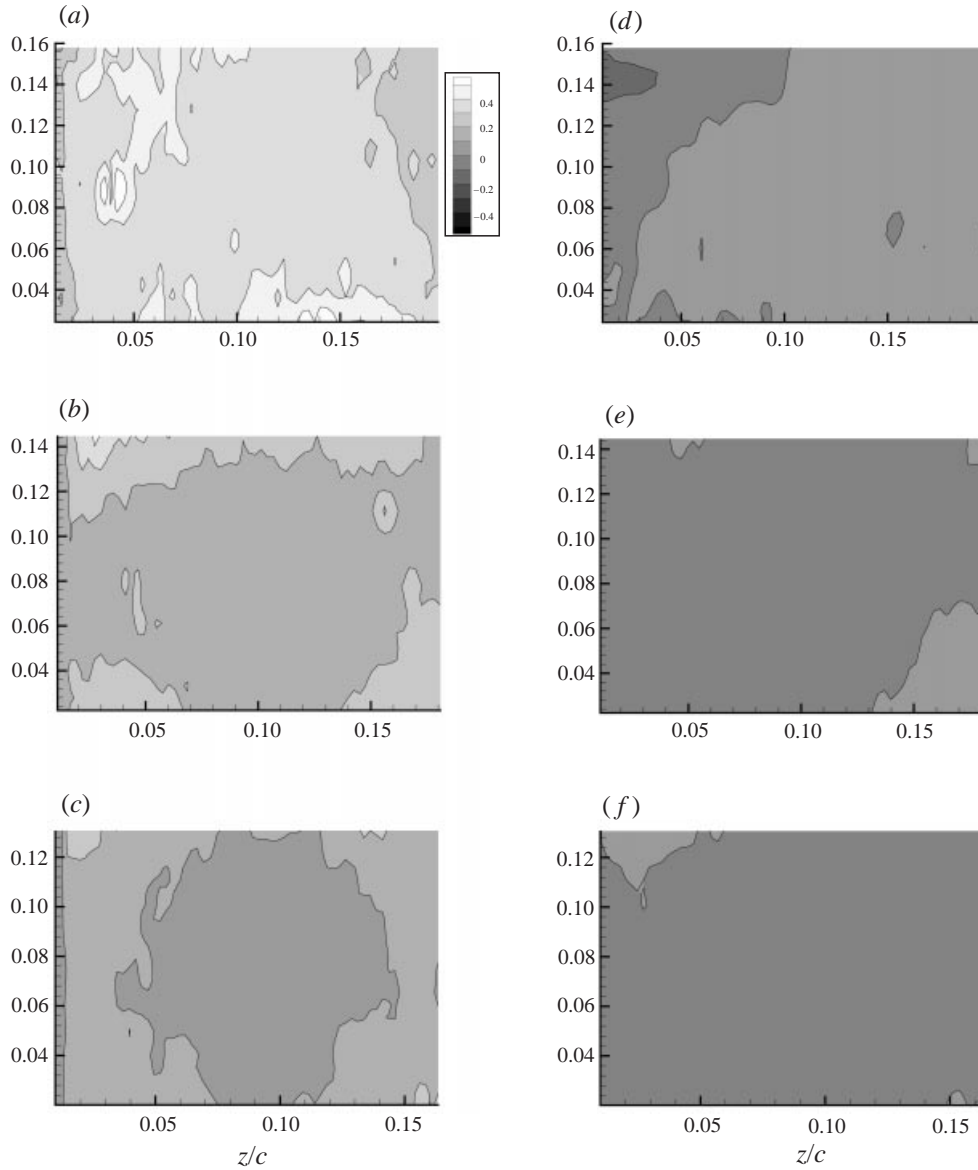
FIGURE 12. Partial sum i.e. sum of terms which could be computed from cross-stream velocity field data) of turbulent kinetic energy dissipation; $x/c = 1.0$ (*a*), 3.5 (*b*), and 7.0 (*c*), and production; $x/c = 1.0$ (*d*), 3.5 (*e*), and 7.0 (*f*).

turbulent kinetic energy production, dissipation, and diffusion profiles were obtain which matched DNS calculations. This Appendix contains a brief uncertainty analysis for the current Δ-wing-vortex mesurements.

It is important to note at the ouset that there are two classes of uncertainty which must be accounted for. The first uncertainty, ϵ is associated with convergence of averages for finite sample sizes. For this class of uncertainties, Lumley & Panofsky (1964) provide the following equation for calculating uncertainties:

$$\epsilon/U_\infty = \{2I(u'/U_{local})^2/T\}^{1/2}, \tag{A 1}$$

where I is the integral time scale of the flow, and T represents the total sampling time. In this case, the integral time scale can be estimated by dividing the core diameter (~ 10 cm) by twice the maximum circumferential velocity (2×15 cm s^{-1}) to obtain a value of 0.33 s. The sampling period is 5000 s and, from the turbulence intensity data shown in figure 8, u'/U_{local} is estimated to be 0.2 Substitution into (A 1) yields a value for ε of 0.034 cm s^{-1}. Note that this is small principally because of the very long sampling time.

The second uncertainty, e, arises from the accuracy and resolution of the DPIV measurement technique. It should be pointed out at the outset that there is a range ofuncertainty estimates in the literature for particle displacement measurements ranging from $O(0.01)$ pixels by Raffel, Willert & Kompanhans (1998) at the low end to the more commonly accepted $O(0.1)$ pixel uncertainty put forward by Keane & Adrian (1992, 1993). It is the authors' opinion that the actual uncertainty for the present measurements is somewhere in between, ~ 0.05 pixels. For the purposes of this discussion, however, the values presented by Raffel *et al.* (1998) and Keane & Adrian (1992) serve as upper and lower bounds for the measurement uncertainty. It should also be noted here that Adrian (1998, personal communication) emphasized that the use of fractional pixel displacement as an uncertainty metric contains an implicit assumption that the mean particle image size is 2–3 pixels which was, in fact, the case for the present measurements.

In their monograph, Raffel *et al.* (1998) identified a number of sources of uncertainty for PIV and DPIV measurement systems. The three relevant uncertainties for this experiment are particle image size in pixels, particle displacement in pixels, and particle image density. Based on the analysis of Raffel *et al.* (1998) and examination of the video images captured in this study, the uncertainties for each of these sources are on the order of 0.01 pixels; the corresponding velocity uncertainty is 0.013 cm s^{-1}. From the work of Kline & McClintock (1953) the combined measurement uncertainty for all three sources of uncertainty is simply the square root of the sum of the squared uncertainties, i.e. $e \approx 0.023$ cm s^{-1}.

As noted earlier, the analysis of Raffel *et al.* (1998) should really be viewed as an idealized estimate. A more commonly accepted estimate developed by Keane & Adrian (1992) among others, is 0.1 pixels. This translates to 0.13 cm s^{-1} for the uncertainty of an instantaneous velocity measurement. Uncertainties of derivative turbulence quantities were then calculated using both the Raffel *et al.* (1998) and Keane & Adrian (1992) analyses and are presented here as upper and lower bounds for the present measurements

To calculate uncertainties in measured and derived quantities, then, a few simple rules were used. First, uncertainties for quantities involving mean velocities were assumed to be functions of ε, while uncertainties of fluctuating velocities were calculated as functions of e. Second, products or quotients of quantities were assumed to have uncertainties equal to the sum of the component uncertainties. Third, uncertainties of sums or differences were equal to the square root of the sum of the squared component uncertainties. Finally, uncertainties associated with derivatives were computed by multiplying the uncertainty of the dependent variable by $\sqrt{2}$ and dividing by the differential length. For central differences, the differential length was twice the vector spacing.

Using these rules, non-dimensional uncertainties were computed for all of the plots presented in the body this paper. These are shown in table 1 including the formulae derived for each quantity. For uncertainties which are functions of e, upper and lower bounds are provided. Non-dimensionalization was done in the same manner as the

Quantity	Formula	Uncertainty range (non-dimensional)
Mean velocity, U_i	ε	0.0023
Turbulence intensities, u'_i	e	0.0015–0.0087
Reynolds stresses, $-\langle u_i u_j \rangle / u'_i u'_j$	$4e$	0.092–0.14
Vorticity advection, $U_j \partial U_j / \partial x_j$	$\varepsilon + \varepsilon/\sqrt{2}(\Delta x)^2$	21.0
Reorientation/stretching, $\Omega_j \partial U_i / \partial x_j$	$(1+1/\sqrt{2})\varepsilon/\Delta x$	5.0
Vorticity diffusion, $\nu \partial^2 \Omega_i / \partial x_j^2$	$\nu\varepsilon/2(\Delta x)^3$	1.5
Anisotropic production, $\partial^2/\partial y \partial z \{\langle v^2 \rangle - \langle w^2 \rangle\}$	$e/\sqrt{2}(\Delta x)^2$	14.0–79.0
Anisotropic production, $\{\partial^2/\partial z^2 - \partial^2/\partial y^2\}\langle vw \rangle$	$\sqrt{2}e/(\Delta x)^2$	28.0–160
TKE dissipation, $\langle \{\partial u_i/\partial x_j + \partial u_j + \partial u_j/\partial x_i\}^2 \rangle$	$2e/\Delta x$	4.0–23.0
TKE Production, $-\langle u_i u_j \rangle \partial U_i / \partial x_j$	$2e + \sqrt{2}\varepsilon/2(\Delta x)$	2.50–2.51

TABLE 1. Computed non-dimensional uncertainties for, all the plots presented in this paper.

corresponding plot. In general, it can be seen that the degree of scatter in the data fall well within the bounds of the limits defined through the works of Raffel *et al.* (1988) and Keane & Adrian (1992). Based on the scatter in the present data, it appears that the velocity measurement uncertainty is somewhat less than 0.05 pixels, or $\sim 0.06\,\mathrm{cm\,s^{-1}}$.

REFERENCES

BATCHELOR, G. K. 1964 Axial flow in trailing line vortices. *J. Fluid Mech.* **20**, 645.

CHOW, J. S., ZILLIAC, G. G. & BRADSHAW, P. 1997 Mean and turbulence measurements in the near field of a wingtip vortex. *AIAA J.* **35**, 1561.

CIPOLLA, K. M. & ROCKWELL, D. O. 1995 Flow structure on stalled delta wing subjected to small amplitude pitching oscillations. *AIAA J.* **33** 1256.

DEVENPORT, W. J., RILE, M. C., LIAPIS, S. I. & FOLLIN, G. J. 1996 The structure and development of a wing-tip vortex. *J. Fluid Mech.* **312**, 67.

GREEN, S. L. & ACOSTA, A. J. 1991 Unsteady flow in trailing vortices. *J. Fluid Mech.* **227**, 107.

GREGA, L. M., WEI, T., LEIGHTON, R. I. & NEVES, J. C. 1995 Turbulent mixed-boundary flow in a corner formed by a solid wall and a free surface. *J. Fluid Mech.* **294**, 17.

HENDERSON, D. O. & SARPKAYA, T. 1985 Free surface scars and striations due to trailing vortices generated by a submerged lifting surface. *AIAA Paper* 85-0445.

HONKAN, A. & ANDREOPOULOS, J. 1997 Instantaneous three-dimensional vorticity measurements in vortical flow over a delta wing. *AIAA J.* **35**, 1612.

HSU, T. Y. 1998 Turbulent transport in the mixed boundary corner formed by flow along a solid wall close to a free surface. MS Thesis, Rutgers University.

KEANE, R. D. & ADRIAN, R. J. 1992 Theory of cross-correlation analysis of PIV images. *Appl. Sci. Res.* **49**, 191.

KEANE, R. D. & ADRIAN, R. J. 1993 Prospects for super-resolution with particle image velocimetry. *Proc. SPIE Optical Diagnostics in Fluid and Thermal Flow* 2005, 283.

KLINE, S. J. & MCCLINTOCK, F. A. 1953 Describing uncertainties in single-sample measurements. *Mech. Engng* **75**, 3.

LEE, M. & HO, C. M. 1990 Lift force of delta wings. *Appl. Mech. Rev.* **43**, 209.

LUMELEY, J. L. & PANOFSKY, H. A. 1964 *The Structure of Atmospheric Turbulence*. Interscience.

MEHTA, R. D. & CANTWELL, E. R. 1998 Mean flow and turbulence measurements in a half-delta wing vortex. *Fluid Dyn. Res.* **4**, 123.

MILLER, G. D. & WILLIAMSON, C. H. K. 1995 Free fight of a delta wing. *Phys. Fluids.* **7**, S9.

MILLER, G. D. & WILLIAMSON, C. H. K. 1997 Turbulent structures in the trailing vortex wake of a delta wing. *Exp. Thermal Fluid Sci.* **14**, 2.

PHILLIPS, W. R. C. 1981 The turbulent trailing vortex during roll-up. *J. Fluid Mech.* **105**, 451.

PRESS, W. H. 1989 *Numerical Recipes: The Art of Scientific Computing.* Cambridge University Press.

RAFFEL, M., WILLERT, C. E., & KOMPENHANS, J. 1988 *Particle Image Velocimetry.* Springer.

SAFFMAN, P. G. 1992 *Vortex Dynamics.* Cambridge University Press.

SHAH, P. N. 1998 The near wake development of the core of a turbulent trailing vortex shed from a delta wing. MS Thesis, Rutgers University.

SHEKARRIZ, A., FU, T. C., KATZ, J. & HUANG, T. T. 1993 Near field behavior of a tip vortex. *AIAA J.* **31**, 112.

SMITH, G. B. 1992 Transport processes in moderate to high Reynolds number vortex rings. PhD Dissertation, Rutgers University.

WENTZ, W. H. & KOHLMAN, D. L. 1971 Vortex breakdown on slender sharp-edged wings. *J. Aircraft.* **8**, 156.

WILLERT, C. E. & GHARIB, M 1991 Digital particle image velocimetry. *Exps. Fluids* **10**, 181.